JMEPEG (2025) 34:16019–16031
https://doi.org/10.1007/s11665-025-11206-5

1059-9495/$19.00

ORIGINAL RESEARCH ARTICLE

Microstructure and Mechanical Properties Evaluation of High Ti-V Microalloyed Steel After Coiling Process at Different Temperatures in a Hot Strip Rolling Simulation Process

Seyed Reza Jafarpour Rezaei, Charles W. Siyasiya, Zhenghua Tang, and Joseph Moema

Submitted: 14 October 2024 / Revised: 11 March 2025 / Accepted: 23 March 2025 / Published online: 9 May 2025

Today, reducing greenhouse gas emissions is a crucial concern, making the development of steel alloys with optimal desired properties and reduced weight an urgent priority, especially in automotive industries, as it leads to decreased fuel consumption, hence the continued interest in developing high-strength low-alloy steels (HSLA). In this research, the impact of coiling temperature on the final microstructure and mechanical properties of Ti-V HSLA microalloyed steel was investigated. The Gleeble 1500 was used to simulate the hot rolling and coiling processes. The results indicated that reducing coiling temperatures led to a transition in microstructures from polygonal ferrite and pearlite to acicular ferrite and bainite. The optimal coiling temperature for achieving high diffusion rates of microalloying elements and optimal precipitation kinetics to form nanosized precipitates was determined to be 650 °C, where the smallest precipitates were observed of 30 nm. However, the specimen subjected to a lower coiling temperature of 550 °C exhibited the highest yield stress (781 MPa), ultimate tensile strength (971 MPa), and hardness (324 HV), which were attributed to microstructural characteristics such as high dislocation density and a finer grain size of 3 μm compared to 6 μm at 700 °C.

Keywords coiling temperature, high Ti-V microalloyed steel, hot strip mill, mechanical properties, microstructure

1. Introduction

Today, the focus lies on the fuel consumption and greenhouse gas emissions particularly in the transport industry. The advancement of alloys characterized by reduced weight and enhanced strength represents a critical area of research focus (Ref 1). This is highlighted by the continued advancements and ongoing research into high-strength low-alloy (HSLA) steels, which have been developed over the past decades and remain a focal point for numerous researchers. Generally, HSLA steels are typically classified as low carbon steels which demonstrate a desirable combination of properties including elevated strength, favorable toughness, good weldability, and exceptional corrosion resistance (Ref 2-5).

There exist several viable approaches to improve the mechanical characteristics of steel alloys, with two of them being particularly effective in attaining the desired properties in HSLA steel (Ref 3, 6). The initial approach involves adding minute quantities of microalloying elements such as titanium (Ti), vanadium (V), niobium (Nb), and molybdenum (Mo). These particular elements enhance the mechanical properties through grain refinement, solid solution strengthening, and precipitation hardening mechanisms (Ref 7-9). Among them, vanadium is favored over other microalloying elements due to reduce hot working temperatures and rolling forces. In Ti-V microalloyed steels, the high solubility of vanadium carbonitride (V(C,N)) allows for easier control of precipitation hardening, particularly in the austenite phase. High Ti-V HSLA steels demonstrate superior mechanical properties, as the combined addition of titanium and vanadium enhances precipitation strengthening by forming fine carbonitride particles. This results in higher yield strength (550-700 MPa) and toughness compared to steels alloyed with only niobium or titanium. Furthermore, titanium's presence alongside vanadium influences the microstructure, affecting hardness and softening behavior. The synergistic effect of these elements provides a well-balanced combination of strength and toughness, making Ti-V HSLA steels ideal for high-performance applications (Ref 8-11).

The second technique involves utilizing the thermomechanical controlled process (TMCP). TMCP is a method extensively used to shape steel while simultaneously improving its mechanical properties by grain refinement and controlling phase transformations (Ref 3). One of the common techniques of TMPC that has been widely applied on HSLA steels is the hot strip mill (HSM) rolling. The HSM rolling process usually consists of several sequential steps including: slab reheating, roughing, finishing rolling, runout cooling, and coiling (Ref

Seyed Reza Jafarpour Rezaei and **Charles W. Siyasiya**, Department of Materials Science and Metallurgical Engineering, University of Pretoria, Pretoria, South Africa; **Zhenghua Tang**, Department of Materials Science and Engineering, Sichuan University, Chengdu, China; and **Joseph Moema**, Advanced Materials Division, Mintek, Randburg, South Africa. Contact e-mail: rezajafarpour2010@gmail.com.

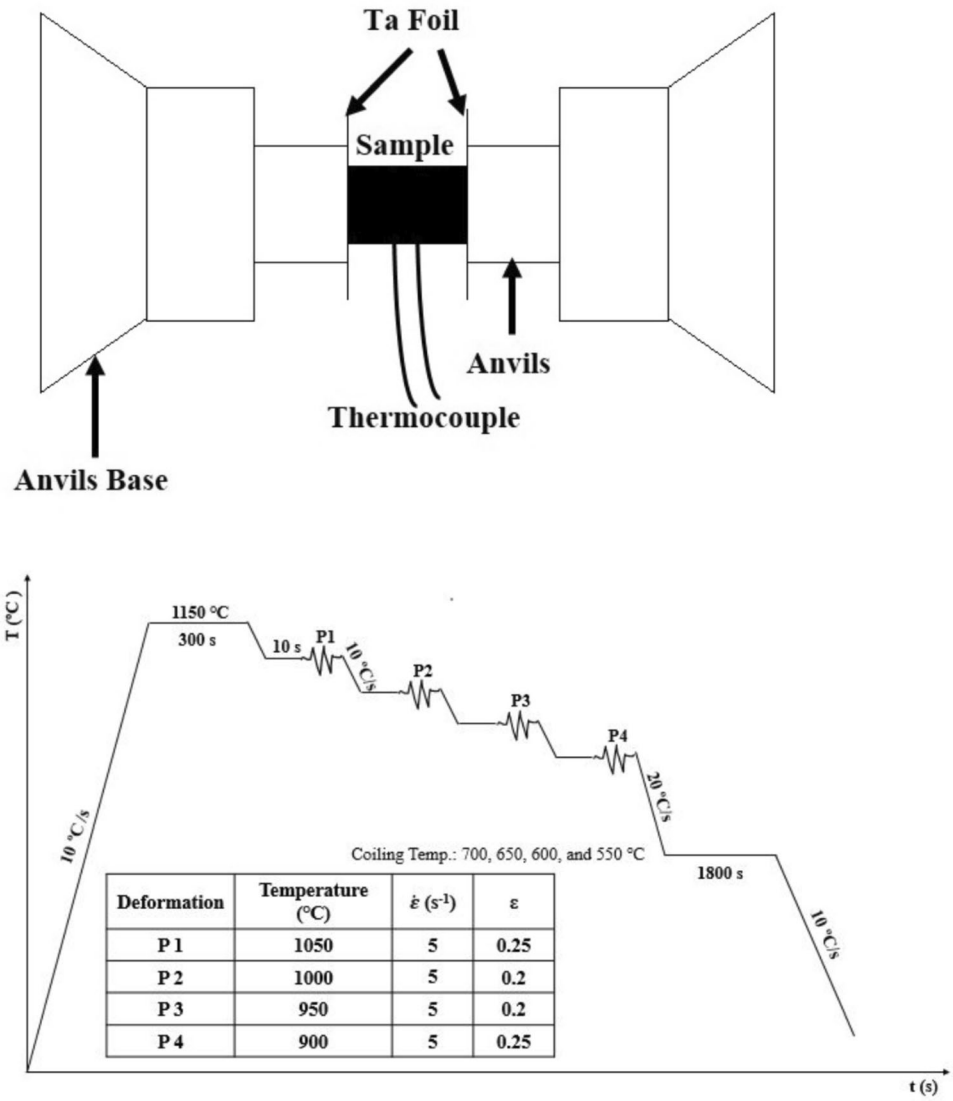

Deformation	Temperature (°C)	$\dot{\varepsilon}$ (s^{-1})	ε
P 1	1050	5	0.25
P 2	1000	5	0.2
P 3	950	5	0.2
P 4	900	5	0.25

Fig. 1 (a) Schematic diagram of the specimen-anvil set-up in the Gleeble machine and (b) thermomechanical process schedule

12). So, it is clear that the process parameters play a significant role in the TMCP as they ultimately impact the material properties. These parameters encompass soaking temperature and time, strain ratio, strain rate, rolling temperature, cooling pattern, and coiling temperature (Ref 13, 14). Consequently, several studies have demonstrated the effect of TMCP parameters such as cooling rate and coiling temperature (CT) on the microstructure, precipitation, and mechanical properties of HSLA steels (Ref 15-19). Olasolo et al. (Ref 18) simulated coiling process in a temperature range of 450-700 °C for 0.062Nb-0.053 V microalloyed steel and found that the maximum hardness was attained at coiling temperature of 600 and 650 °C. Lei et al. (Ref 19) focused on 0.094Ti-0.078Nb microalloyed steel and demonstrated that a lower coiling temperature supplied sufficient driving force for the precipitation while restraining precipitate coarsening.

Given that the coiling temperature is the most cost-effective and efficient approach for enhancing the properties of microalloyed steels during the TMPC process (Ref 13), this study examined the effect of the coiling temperature in a TMCP process on the mechanical properties and microstructure of high Ti-V microalloyed steel. The results obtained provide a fundamental basis for the development of Ti-V HSLA steels.

2. Material and Experimental Method

The chemical composition of the investigated high Ti-V steel alloy was 0.14%C, 0.44%Si, 1.62%Mn, 0.13%V, 0.1%Ti, 0.02%S, 0.02%P, 0.005%N, and 0.62%Cr (in mass%). Figure 1 illustrates the TMCP simulation. Cylindrical test samples with a diameter of 10 mm and a height of 15 mm were machined from the initial ingot, and hot strip rolling was simulated using the Gleeble 1500^{TM} thermomechanical simulation machine. The samples were first reheated to 1150 °C at a heating rate of 10 °C/s, held for 300 s, and then cooled to the initial rolling temperature of 1050 °C at a cooling rate of 10 °C/s. Upon reaching the deformation temperature, the samples were held for 10 s before being subjected to a strain of 0.25. Subsequently, the samples were cooled to the second, third, and fourth deformation temperatures (1000, 950, and 900 °C,

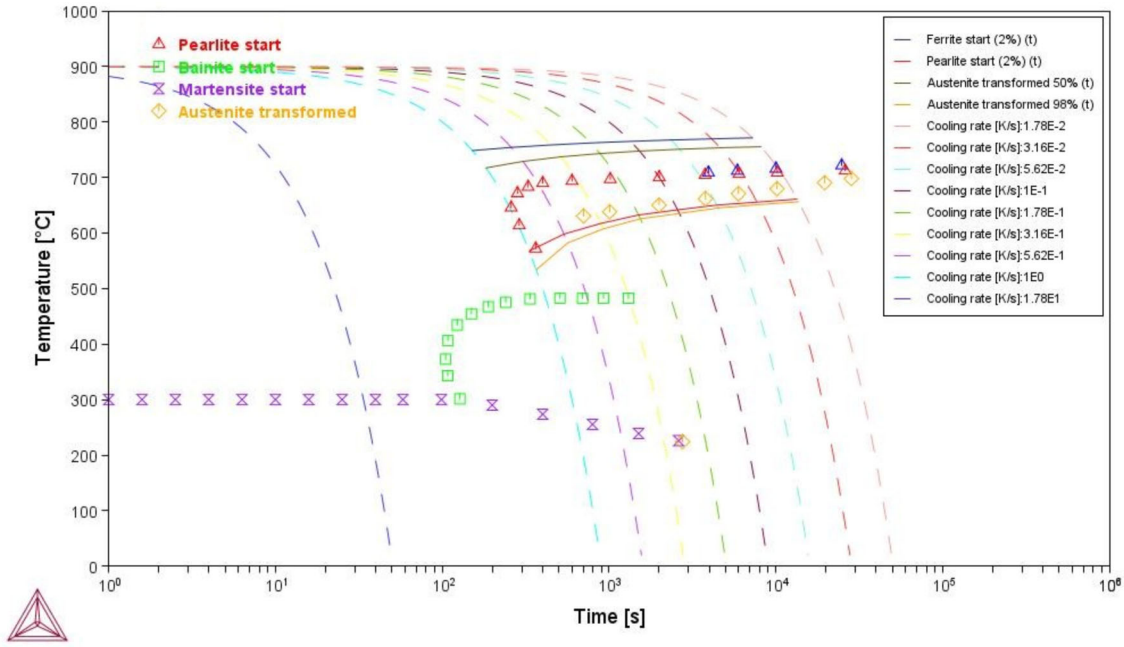

Fig. 2 Continuous cooling transformation diagram of the experimental steel calculated using Thermo-Calc software

respectively) and deformed with strains of 0.2, 0.2, and 0.25, respectively, at a strain rate of 5 s^{-1}. After the final deformation pass, the specimens were continuously cooled to coiling temperatures of 700, 650, 600, and 550 °C at a cooling rate of 20 °C/s. They were held at these temperatures for 1800 s to simulate the coiling process, after which they were cooled to room temperature at a cooling rate of 10 °C/s.

To study the microstructure evolution, the specimens were sectioned into two halves parallel to the compression axis. The cross-sectional surface was prepared according to standard metallographic techniques, etched in 4% Nital, and the microstructure was observed by an Olympus BX51MTM optical microscope. The phase fraction was determined using ImageJ software, where the thresholding tool was applied to distinguish individual phases, based on contrast variation. To improve statistical reliability, at least six images were analyzed for each coiling temperature. The samples were further polished with silica colloidal (0.05 μm) solution to achieve a higher quality EBSD maps. The EBSD maps were obtained in a 0.25 μm step size in RD-ND plane, using a scanning electron microscope (SEM-JSM-IT300 JEOL) equipped with an Oxford EBSD detector and the Channel 5 software. Both the SEM-EDS and the transmission electron microscopy (TEM) were employed to characterize precipitates. The SEM-EDS was used to characterize the large size precipitate which were stable at soaking temperature. The TEM was used to characterize nano-scale precipitates by carbon replica extraction method. The carbon replicas were examined by the JEOL 2100F FEG TEM equipped with EDS detector at 200 kV.

Hardness test and profilometry-based indentation plastometry (PIP) test were employed in order to investigate the mechanical properties. A total of fifteen hardness values were recorded along the central surface of the samples in order to ascertain the mean hardness values. The yield stress, ultimate tensile stress (UTS), and uniform elongation of samples were derived through the application of the PIP testing methodology (Ref 20).

3. Results and Discussion

3.1 Microstructure

Figure 2 shows the continuous cooling transformation (CCT) diagram of experimental steel calculated by Thermo-Calc software. A grain size of 20 μm after austenitization at 900 °C was assumed (Ref 13, 19). It can be seen from the CCT curve that the ferrite and pearlite start temperatures were predicted to be 790 and 680 °C, respectively. As can be seen, the microstructures were predicted to be mainly ferrite and pearlite at most cooling rates.

Figure 3(a), (b), (c), and (d) depicts optical micrographs captured at various coiling temperatures within the middle section of the examined steel's thickness. Observing the optical micrographs, it becomes evident that at higher CT (700 and 650 °C), the final microstructure of the samples primarily comprises polygonal ferrite (PF) and pearlite (P), with fewer instances of granular ferrite (GF), as labeled in Fig. 2(a) and (b). At a CT of 600 °C, the PF and P remain prominent part of microstructure, but the acicular ferrite (AF) begins to emerge. At lower CT of 550 °C, the microstructure undergoes significant changes, by the formation of acicular ferrite and bainite (B) as prominent phases, Fig. 2(d). The phase fraction analyses are summarized in Fig. 3(e), showing a decrease in P fraction with CT.

Lowering the CT retards the transformation of austenite into ferrite and pearlite. It has been found that, lower CTs obstruct the formation of polygonal ferrite and pearlite, while encouraging the transformation of acicular ferrite and bainite. This is because lower CTs suppress the diffusion-controlled transformation of polygonal ferrite and pearlite. Lower CTs do not only decrease the diffusion rate of carbon, but also restrict the mobility of substitutional alloying elements such as Mn, Ti, and V. Consequently, these elements accumulate at austenite grain boundaries, enhancing the solute drag effect, which delays the

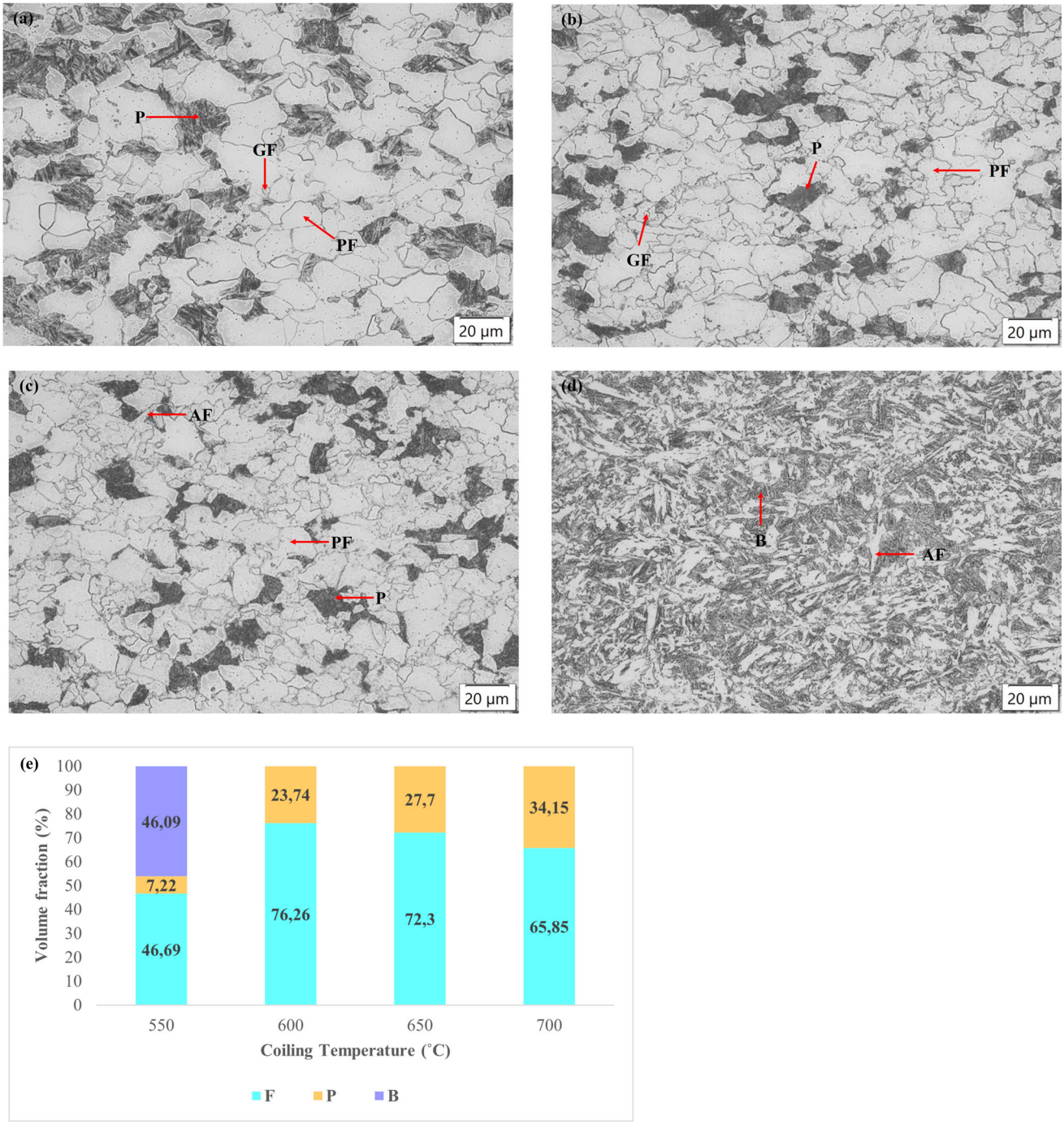

Fig. 3 Optical micrographs of the investigated samples for coiling temperatures of (a) 700, (b) 650, (c) 600, and (d) 550 °C, and (e) the volume fraction of different phases after coiling process. (Polygonal Ferrite (PF), Acicular Ferrite (AF), Granular Ferrite (GF), Pearlite (P), and Bainite (B))

formation of polygonal ferrite and pearlite while favoring the formation of acicular ferrite and bainite (Ref 21, 22).

3.2 EBSD

Figure 4 displays the inverse pole figure (IPF) map corresponding to the longitudinal section of the deformed samples after coiling simulation. Not only a random orientation is observed but also a non-uniform distribution of grain size was also observed. Inhomogeneous nucleation and growth of ferrite grain, during phase transformation from austenite to ferrite, is a reason for the non-uniform grain size distribution (Ref 23). Figure 5 shows the grain boundary maps. The high-angle grain boundaries (HAGBs), characterized by grain misorientation exceeding 15°, and the low-angle grain boundaries (LAGBs), with grain misorientation between 2° and 15°, were marked by black and red line, respectively. The volume fraction of LAGBs increased with a decrease in coiling temperature. In other words, the minimum CT (550 °C) showed the highest density of LAGB, indicating a higher

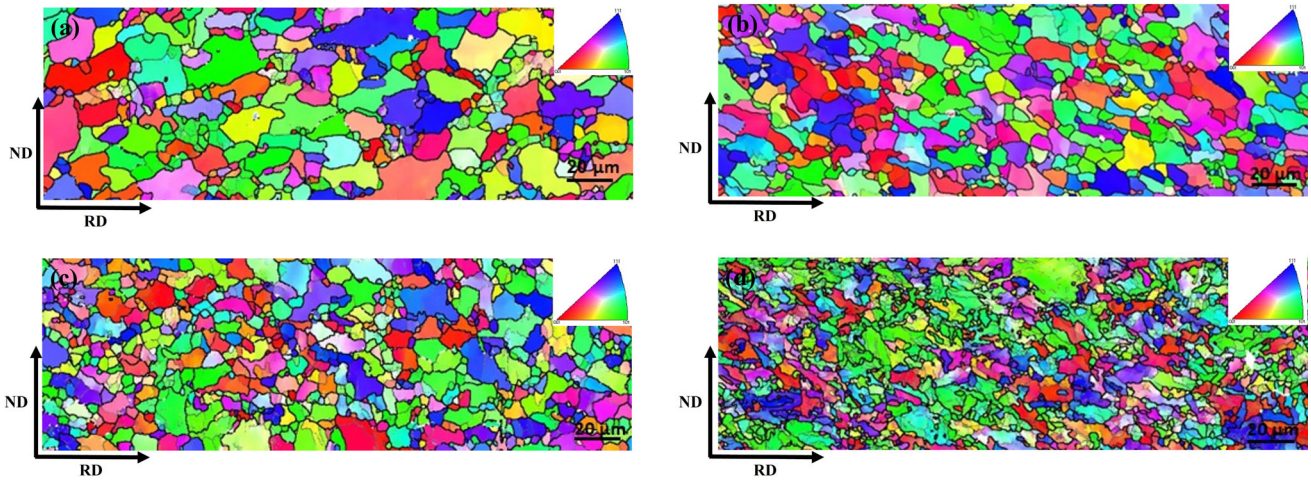

Fig. 4 The IPF maps taken from longitudinal section after coiling simulation at (a) 700, (b) 650, (c) 600, and (d) 550 °C

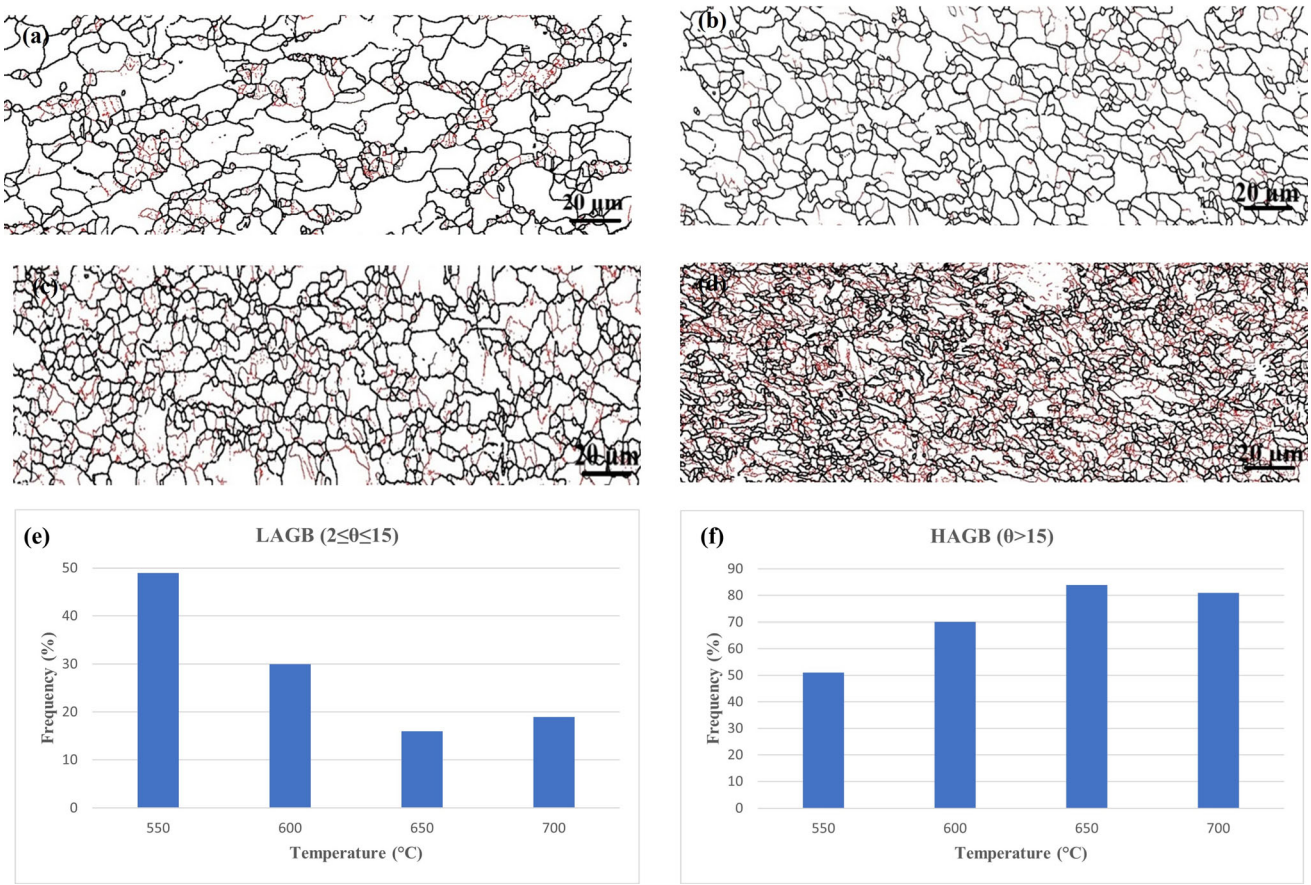

Fig. 5 Grain boundary maps, with low-angle grain boundaries ($2° \leq \theta \leq 15°$), represented in red, and high-angle grain boundaries ($\theta > 15$) in black for (a) 700, (b) 650, (c) 600, and (d) 550 °C, and (e) and (f) fraction of low-angle grain boundaries and high-angle grain boundaries, respectively

dislocation density likely resulting from static recovery during the coiling process (Ref 24).

Figure 6 shows the average grain size and distribution. As may be seen, approximately 80% of the grains are smaller than 10 μm, while coarser grain ($\geq$ 15 μm) can be found in specimens subjected to high coiling temperature. This shows that the CT has a significant influence on grain refinement in these steels. The decrease in CT from 700 to 600 °C resulted in a slight reduction in the average grain size while a further decrease to 550 °C resulted in drastic decrease in grain size. In other words, the average grain sizes were found to be 7 and 3.8 μm at CTs of 700 and 550 °C, respectively.

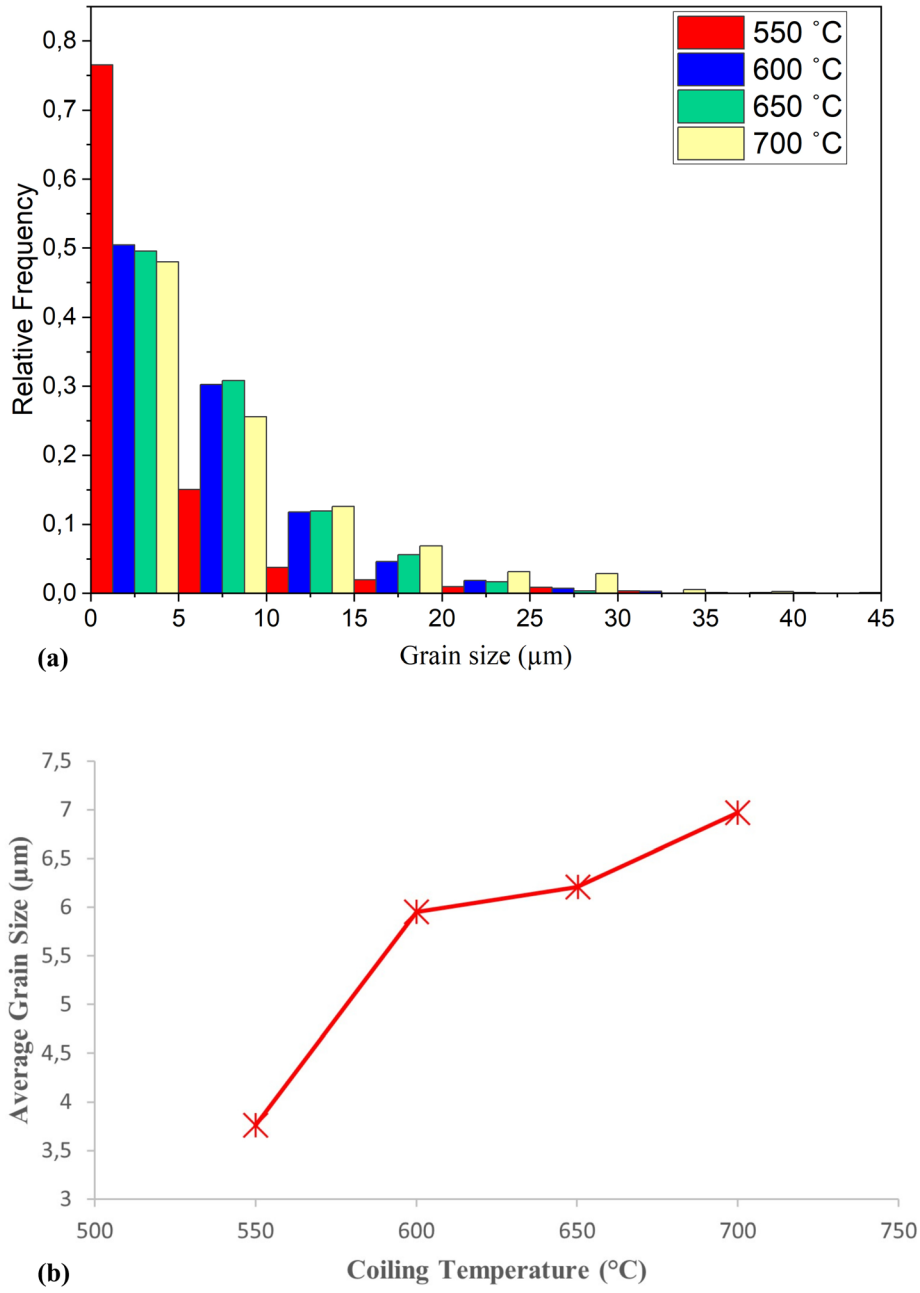

Fig. 6 (a) Grain size distribution and (b) average grain size as function of coiling temperature.

3.3 Precipitation Behavior

The precipitation behavior was modeled using Thermo-Calc software, Fig. 7. As may be seen, the precipitates can be categorized into three distinct groups. First group of precipitates form in the molten metal, e.g., TiN, and are mostly coarse. The second category forms in the austenite phase during slab reheating, e.g., $Ti_4C_2S_2$, and the third type forms at low temperature, i.e., during the austenite to ferrite phase transformation, e.g., VC.

Figure 8 shows the morphology and type of precipitates after reheating at 1150 °C. As may be seen, four different types of precipitates were observed, Type I and Type II refer to the TiN and MnS, respectively. These types of precipitates are too large to effectively hinder coarsening of the austenite grains during reheating and also have no impact on the recrystallization of austenite grains during hot working. Type 3 consists of spherical $Ti_4C_2S_2$ and TiC, and was rarely found in microstructure after soaking. In contrast with Types 1 and 2, $Ti_4C_2S_2$ and TiC precipitates effectively impede the growth of austenite grains and the occurrence of recrystallization during the reheating and hot working processes (Ref 25, 26).

Figure 9a depicts TiN particles at 650 °C. The TiN was found to nucleate preferentially on the aluminum oxide. Figure 9(b) presents the average size of TiN particles with respect to the coiling temperature. The average size of the TiN particles was found to be 5 μm regardless of the coiling temperature. This suggests that the size of TiN particles remains

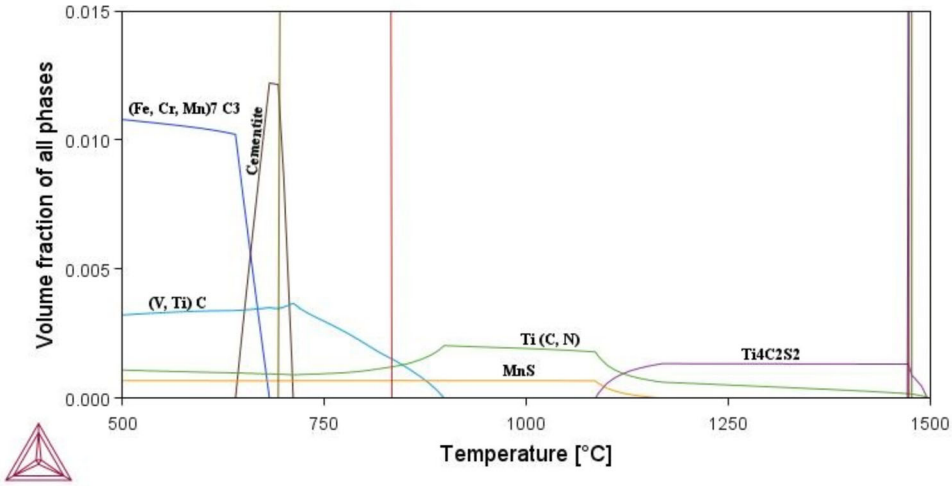

Fig. 7 Thermo-Calc prediction of precipitate formation

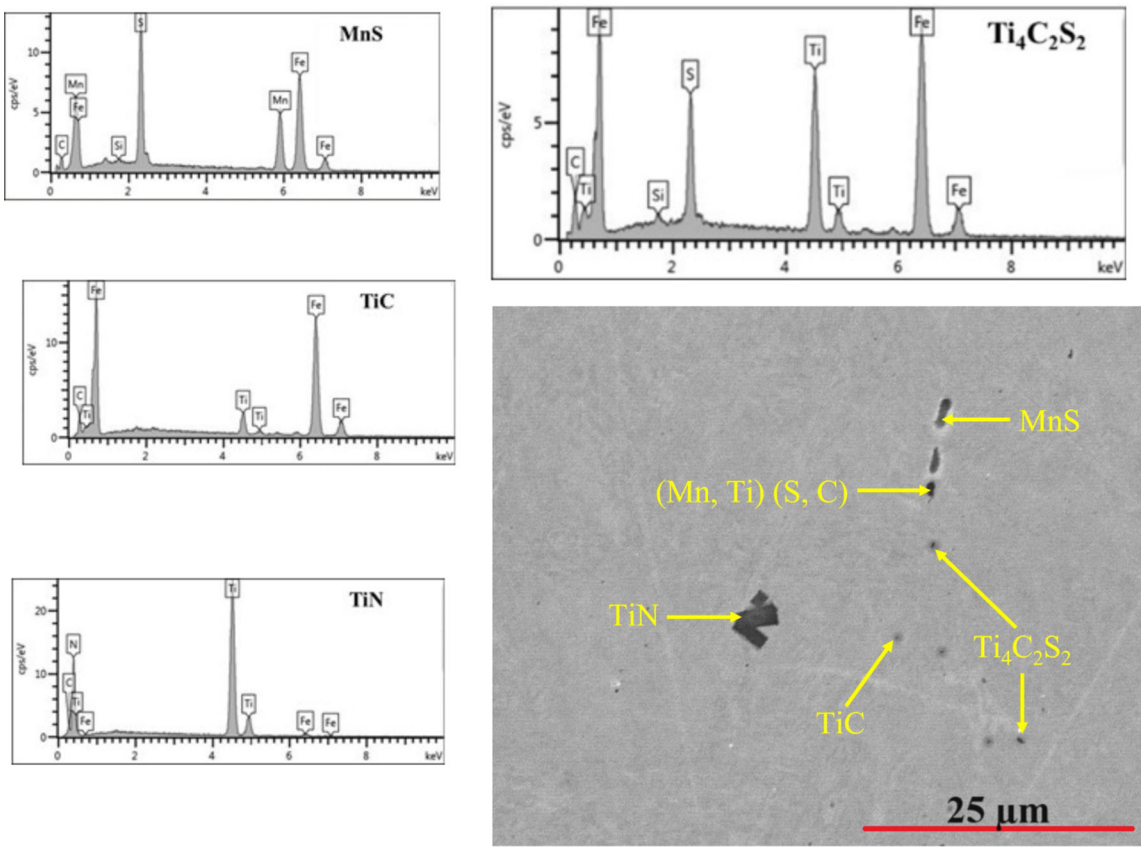

Fig. 8 Precipitates morphology and type after reheating samples at 1150 °C for 300 s and the related EDS spectra

relatively constant regardless of coiling temperature since they form at elevated temperatures.

The solid solubility of the carbide and nitride particles in microalloyed steel can be articulated using the following formula (Ref 27):

$$\log\{[M]\cdot[X]\} = A - B/T \quad \text{(Eq 1)}$$

where [M] and [X] represent the equilibrium solubility in mass percent of V or Ti and C or N, respectively; T is absolute temperature in K; and A and B are specific constant in austenite and ferrite matrix.

Equation 2, 3, 4, 5, and 6 express equilibrium solid solubility of TiN, TiC, and VC in austenite and ferrite (Ref 28, 29):

$$\log\{[Ti]\cdot[N]\}_{\gamma} = 3.94 - 15190/T \quad \text{(Eq 2)}$$

$$\log\{[Ti]\cdot[C]\}_{\gamma} = 5.33 - 10475/T \quad \text{(Eq 3)}$$

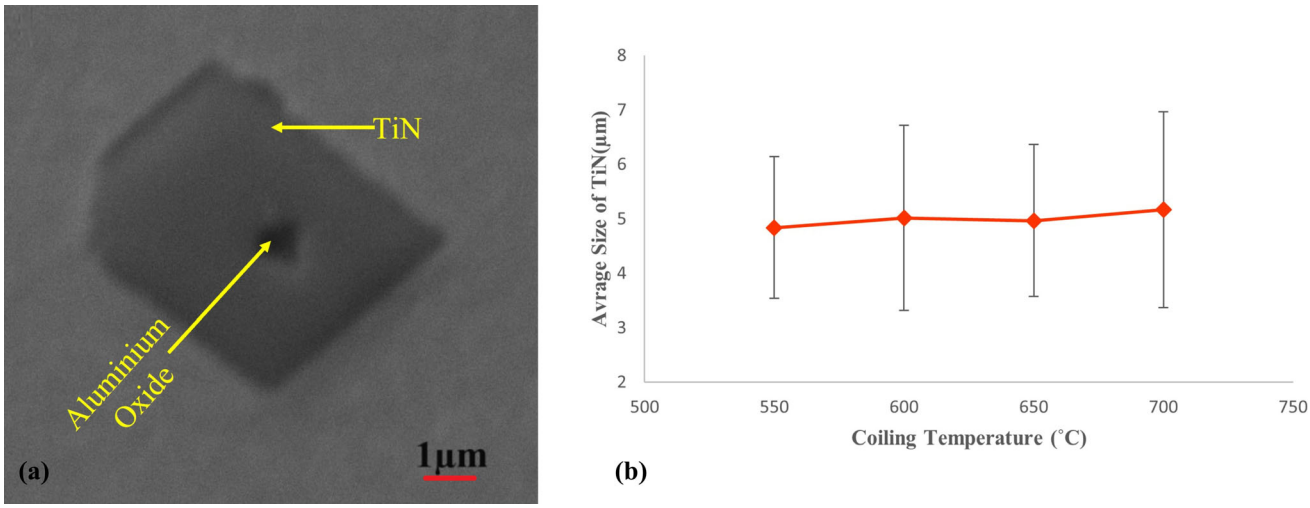

Fig. 9 (a) TiN morphology at coiling temperature 650 °C and (b) TiN average size according to coiling temperature

$$\log\{[Ti]\cdot[C]\}_{\alpha} = 4.40 - 9575/T \quad \text{(Eq 4)}$$

$$\log\{[V]\cdot[C]\}_{\gamma} = 6.72 - 9500/T \quad \text{(Eq 5)}$$

$$\log\{[V]\cdot[C]\}_{\alpha} = 8.05 - 12265/T \quad \text{(Eq 6)}$$

where [Ti], [V], [C], and [N] are the solid solution amount of element Ti, V, C, and N, γ and α represent austenite and ferrite, respectively. According to the TMCP schedule (Fig. 1), the steel was soaked at 1150 °C for 300 s. At this temperature, the solubility of TiN was calculated as 1.86×10^{-7}, i.e., the TiN particles were stable at soaking temperature and because of their large size had minor contribution to the recrystallization of austenite grain during TMCP, and, consequently, have minimal impact on the final mechanical properties. On the contrary, the solubility of TiC and VC particles was calculated as 9.30×10^{-3} and 1.10, which indicates that the majority of TiC particles and all VC particles dissolved at soaking temperature of 1150 °C. These particles reprecipitated during the TMCP and coiling process.

Figure 10 displays the TEM carbon extraction replicas of the precipitates. Three distinct types of precipitates can be observed, namely, large $Ti_4C_2S_2$, TiC, and VC. These precipitates vary in size from 5 to 260 nano-meters and are distributed irregularly and randomly. In this study, it was discovered that fine VC and TiC particles formed during the deformation and coiling process, whereas TiN and $Ti_4C_2S_2$ remained stable at the soaking temperature, which explains their large size. The particle size distribution, average diameter, and volume fraction of precipitates are illustrated in Fig. 11. At lower coiling temperature of 550 °C, the size of precipitates was found to be significantly large, while simultaneously exhibiting the lowest volume fraction of precipitates. This occurrence can be attributed to the fact that the formation of precipitates is primarily controlled by atomic diffusion and the diffusion rate, both of which were hindered by the reduced coiling temperature of 550 °C and for 1800 s. Consequently, the nucleation of TiC and VC was constrained, leading to the retention of a substantial amount of V, Ti, and C atoms in the solution at lower coiling temperatures under the investigated conditions. Conversely, the smallest size and a larger volume fraction of precipitates were achieved at a coiling temperature of 650 °C, indicating a heightened nucleation rate of precipitates at this particular temperature, i.e., the TTT noise of the precipitation process.

3.4 Mechanical Properties

The hardness and tensile properties obtained from the PIP test are summarized in Table 1. It can be seen that the modeled yield strength continuously increases as the CT decreased. Meanwhile, the UTS initially decreased, then increased, and the elongation showed a zigzag pattern: It first decreased, and then increased, and finally, drops sharply as the CT decreased.

Various strengthening mechanisms including lattice friction stress (σ_0), solid solution strengthening (σ_s), grain boundary strengthening contribution (σ_g), dislocation strengthening contribution (σ_d), and precipitation strengthening contribution (σ_p) play a role in determining the final yield strength (σ_y) (Ref 7, 30, 31). The lattice friction stress can be considered the same for all samples, and it is approximately equal to 48 MPa for HSLA steels (Ref 32).

The solid solution strengthening and the precipitation strengthening can be expressed by the following equation (Ref 1):

$$\sigma_p = \frac{5.9\sqrt{f}}{d}\ln\frac{d}{2.5\times10^{-10}} \quad \text{(Eq 7)}$$

where d and f present the average diameter and volume fraction of the precipitates, respectively.

According to Eq. 7, the presence of fine precipitates with a high-volume fraction significantly contributes to the mechanism of precipitation strengthening. As per the previously discussed TEM results, precipitation strengthening was expected to be predominant in the steel coiled at 650 °C. However, the mechanical properties indicate that the sample coiled at 550 °C exhibited the highest YS and UTS. This contradiction suggests that other mechanisms must be at play one of them being the solid solution strengthening. This contribution can be described by the following expression (Ref 31):

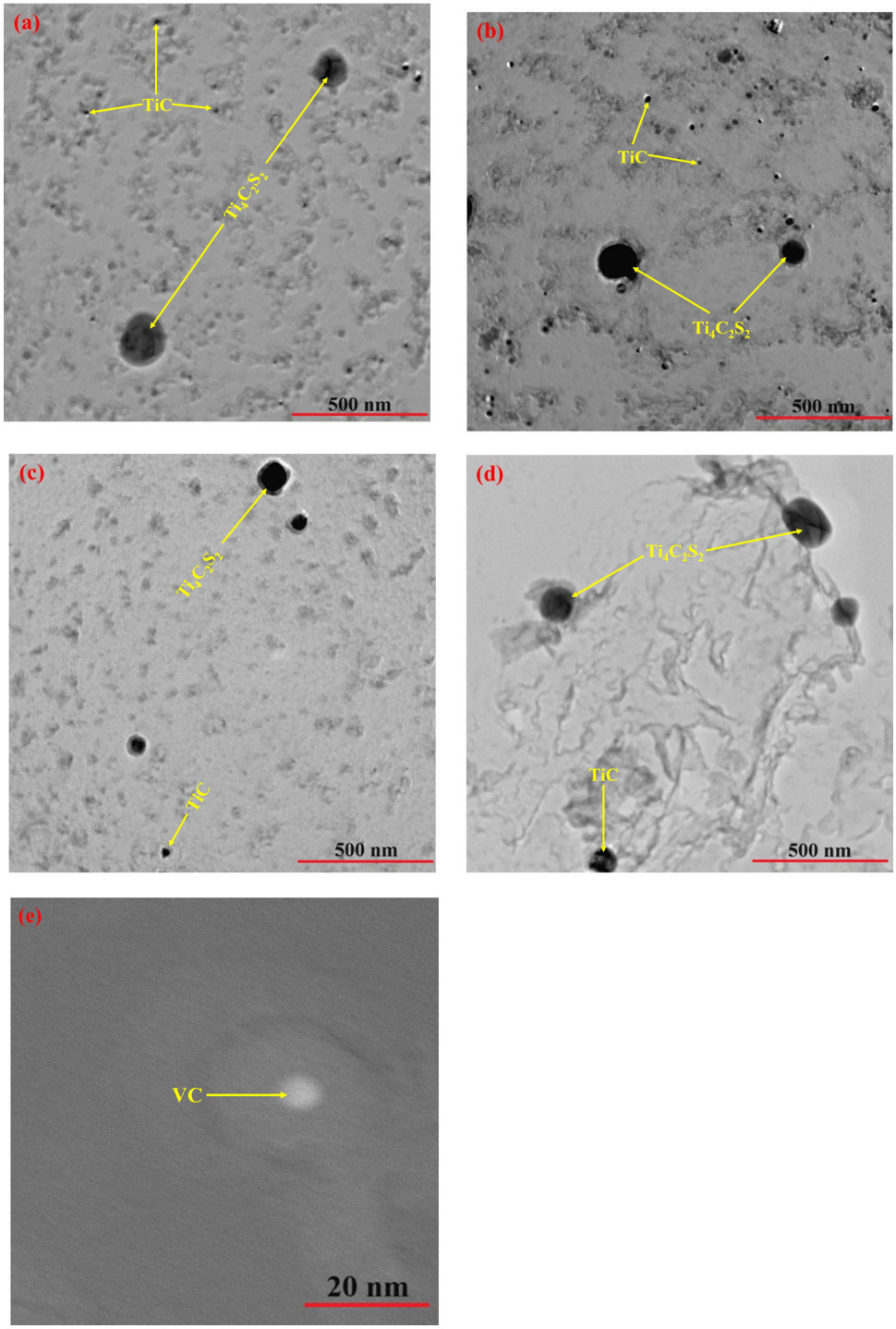

Fig. 10 TEM micrograph of precipitates and related EDS spectra at coiling temperature (a) 700, (b) 650, (C) 600, and (d) 550 °C, and (e) VC morphology at coiling temperature 700 °C (dark field image)

$$\sigma_s = 4570[C] + 3750[N] + 37[Mn] + 83[Si] + 470[P] + 2.9[V] + 80[Ti + Nb] + 11[Mo] - 30[Cr] \quad \text{(Eq 8)}$$

Here [M] is the mass fraction of element in solid solution in the ferrite phase. During the reheating process, a considerable quantity of alloying elements dissolve into the austenite phase, such as Ti, V, and C. Subsequently, during cooling to coiling temperature and coiling process, these elements are expected to precipitate as fine TiC and VC. However, the study of precipitation behavior revealed that as the coiling temperature decreases, the volume fraction of precipitates also decreases, this resulted in a significant amount of alloying elements remaining in a solid solution, which increase both the YS and UTS through solid solution strengthening.

Two additional mechanisms that impact the final yield strength of the tested steel are grain boundary strengthening and

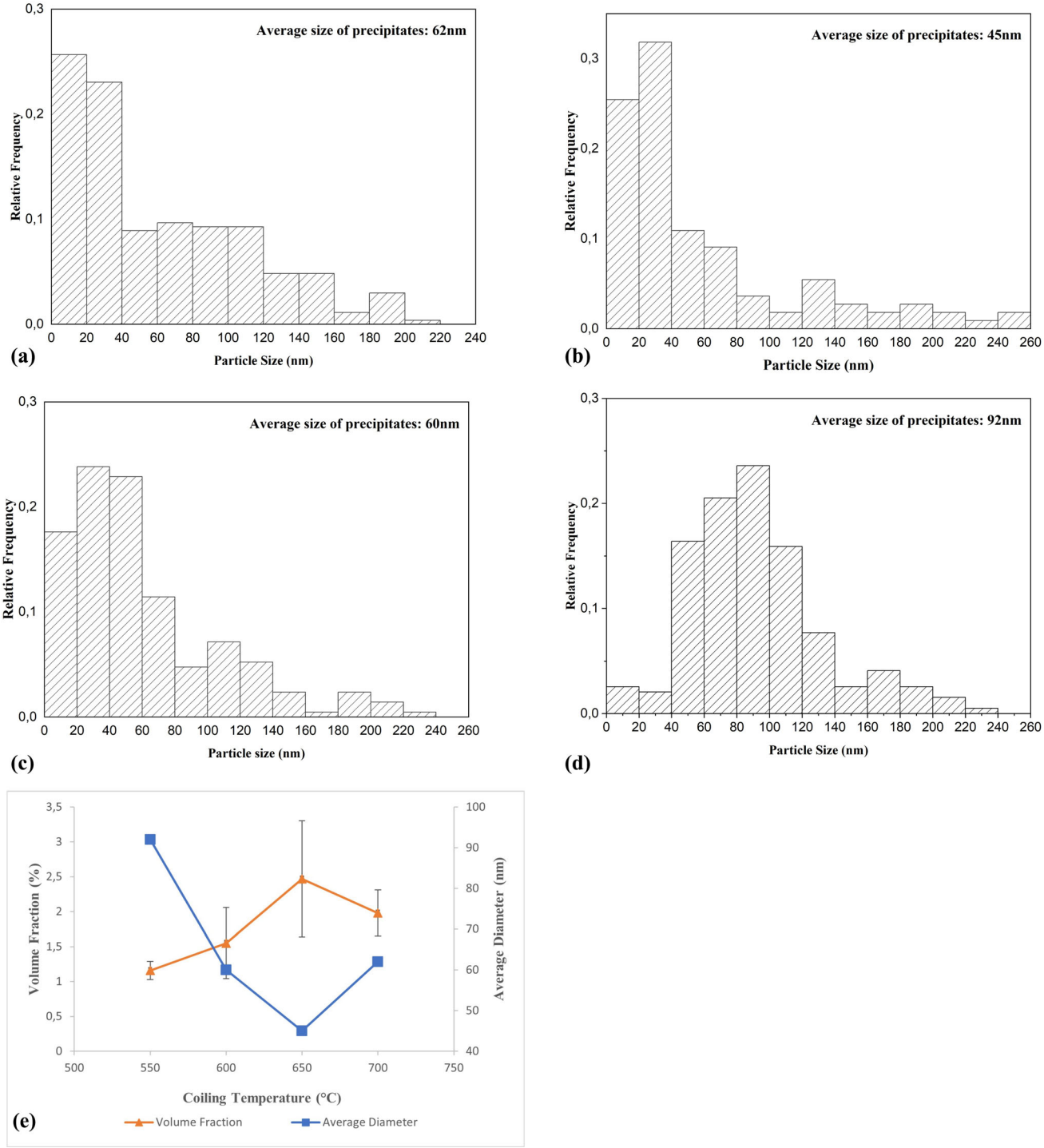

Fig. 11 Particle size distribution at different coiling temperatures, (a) 700, (b) 650, (c) 600, and (d) 550 °C, and (e) average particle size and volume fraction of particles as function of the CT

dislocation strengthening, both of which depend on the microstructure.

The mechanical properties of polycrystalline metals at low temperatures are influenced by the grain boundaries through the Hall–Petch relationship (Ref 33, 34):

$$\sigma_g = \frac{k}{\sqrt{d}} \qquad \text{(Eq 9)}$$

where K is the constant, and for HSLA steel, this parameter is equal to 0.55 MPa.m0.5 (Ref 35), and d is average grain size (m). The results of the grain size analyze, as illustrated in Fig. 6(b), indicate a decrease in the average grain size from 7 to 3.76 μm as the coiling temperature dropped from 700 to 550 °C. This reduction in coiling temperature resulted in an approximately 36 percent increase in the contribution of grain boundaries to the strengthening mechanism.

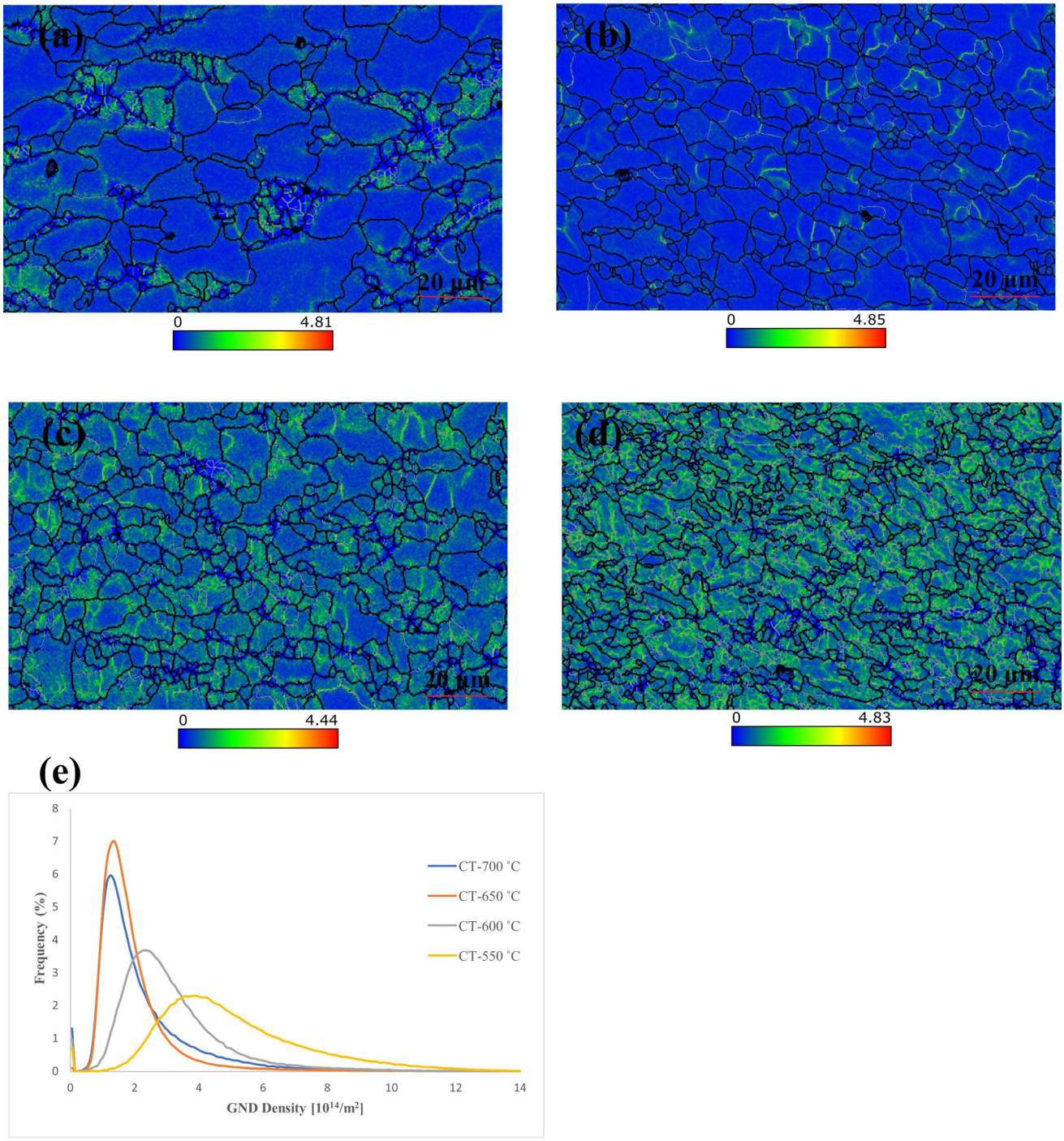

Fig. 12 KAM maps at coiling temperatures of (a) 700, (b) 650, (c) 600, and (d) 550 °C, and (e) GND distribution

The dislocation density, as structural factor, contributes to an increase in YS and UTS through dislocation interactions. These interactions can lead to the formation of dislocation tangles, that impede the movement of dislocations leading to dislocation strengthening (Ref 36, 37):

$$\sigma_d = \alpha M G b \rho^{0.5} \quad \text{(Eq 10)}$$

where α is the crystal structure constant and equals to 0.38, M is the Tylor factor and equals to 2.2, and G is the shear modulus (81,600 MPa), and b is the Burgers vector (2.5×10^{-10} m), and ρ is the dislocation density.

In deformed polycrystalline metals, dislocation can be categorized as geometrical necessary dislocation (GND_S) and statistically stored dislocation (SSD_s) (Ref 38, 39). The GNDs can be analyzed using EBSD because they are directly proportional to the kernel average misorientation (KAM) (Ref 40). The relationship between GNDs and the KAM is given by (Ref 38, 41):

$$\rho_{GNDs} = \frac{\alpha\theta}{ub} \quad \text{(Eq 11)}$$

Table 1 Mechanical properties of samples after coiling

Coiling temperature (°C)	Hardness, HV	Yield stress, MPa	UTS, MPa	EL, %
700	246 ± 9	466 ± 66	897 ± 11	18.23 ± 0.7
650	248 ± 10	591 ± 19	785 ± 12	15.60 ± 0.5
600	288 ± 19	611 ± 35	955 ± 27	18.02 ± 0.2
550	324 ± 7	781 ± 16	971 ± 20	13.59 ± 0.7

Here u is the unit length, θ is the kernel average misorientation, b is the burgers vector (2.5×10^{-10} m), and α is a constant that depends on the kind of dislocation boundaries. The KAM maps and GNDs' distribution curve for the tested steel are given in Fig. 12. The KAM maps demonstrate that as coiling temperature decreases, the KAM magnitude rises, which corresponds to an increase in the average GNDs, that aligns with Eq. 11. This increase in dislocation density was anticipated due to the reduction in static recrystallization and the formation of acicular ferrite with decreasing coiling temperature. This led to an increase in YS and UTS with decreasing coiling temperature.

The investigation into mechanical properties, microstructure, and precipitation behavior revealed that structural parameters, such as average grain size and dislocation densities, have a notable effect on the final mechanical properties, in comparison with the precipitation strengthening mechanism. And these parameters are significantly influenced by the coiling temperature.

4. Conclusions

The evolution of the microstructures and mechanical properties in high Ti-V microalloyed steel after hot rolling and coiling simulations were investigated, and the following conclusion were drawn:

- The microstructures were found to be polygonal ferrite and pearlite in various proportions depending on the coiling temperature between 700 and 600 °C. However, when the coiling temperature was dropped to 550 °C, the microstructures were found to be predominantly acicular ferrite and bainite.
- The TiN was already coarse at both soaking and coiling temperatures since it formed at high temperature and, therefore, had no significant effect on the evolution of the microstructures during the downstream processing.
- The results indicated that the precipitation and volume fraction of precipitates were highly dependent on the coiling temperature. This is because the nucleation of precipitates relies on the diffusion process, which is significantly influenced by temperature. The optimal coiling temperature for achieving fine precipitates with a high-volume fraction was 650 °C. At 550 °C, however, the low diffusion rate restricted the formation of fine precipitates in ferrite during the coiling process.
- In general, the mechanical properties improved with a decrease in coiling temperature. This was due to the formation of AC ferrite and B, as well as the higher dislocation density in samples at lower coiling temperatures.

Acknowledgments

This work was financially supported by the Advanced Materials Initiative (AMI) of the Department of Science and Innovation (DSI) through Mintek. The authors also acknowledge the University of Pretoria for providing the research facilities.

Funding

Open access funding provided by University of Pretoria.

References

1. X. Zhang, C. Loannidou, G.H. de Brink, A. Navarro López, J. Wormann, J. Campaniello, R.M. Dalgliesh, A.A. van Well, S.E. Offerman, W. Kranendonk, and B.J. Kooi, Microstructure, Precipitate and Property Evolution in Cold-Rolled Ti-V High Strength Low Alloy Steel, *Mater. Des.*, 2020, **192**, p 1–13.
2. P. Gong, E. Palmiere, and W. Rainforth, Thermomechanical Processing Route to Achieve Ultrafine Grains in Low Carbon Microalloyed Steels, *Acta Mater.*, 2016, **119**, p 43–54.
3. A. Zavdoveev, V. Poznyakov, T. Baudin, M. Rogante, H.S. Kim, M. Heaton, Y. Demchenko, V. Zhukov, and M. Skoryk, Effect of Heat Treatment On the Mechanical Properties and Microstructure of HSLA Steels Processed by Various Technologies, *Mater. Today Commun.*, 2021, **28**, p 1–12.
4. A. Qaban, T. Mohmed, M. Quazi, and S. Naher, The Effect of Al and Nb Contents, Cooling Rate and Rolling Condition on the Microstructure and Corrosion Behaviour of HSLA Steel, *Mater. Today Commun.*, 2022, **25**, p 1–11.
5. X. Wang, Z.-C. Wang, X.-B. Wang, Y.-R. Wang, J.-Q. Gao, and X.-L. Zhao, Effect of Cooling Rate and Deformation on Microstructures and Critical Phase-Transformation Temperature of Boron-Nickel Added HSLA H-Beams, *J. Iron. Steel Res. Int.*, 2012, **19**, p 62–66.
6. A. Bakkaloglu, Effect of Processing Parameters on the Microstructure and Properties of an Nb microalloyed Steel, *Mater. Lett.*, 2002, **56**, p 200–209.

7. L.G. Sesma, B. Lopez, and B. Pereda, Effect of Coiling Conditions on the Strengthening Mechanisms of Nb Microalloyed Steels with High Ti Addition Levels, *Mater. Sci. & Eng. A*, 2019, **748**, p 386–395.
8. W. Hui, Y. Zhang, C. Shao, S. Chen, X. Zhao, and H. Dong, Effect of Cooling Rate and Vanadium Content on the Microstructure and hardness of Medium Carbon Forging Steel, *J. Mater. Sci. Technol.*, 2016, **32**, p 545–551.
9. Y. Tian, Q. Li, Z.-D. Wang, and G.-D. Wang, Effects of Ultra Fast Cooling on Microstructure and Mechanical Properties of Pipeline Steels, *J. Mater. Eng. Perform.*, 2015, **24**, p 3307–3314.
10. S. Zajac, T. Siwecki, W.B. Hutchinson, and R. Lagneborg, Strengthrning Mechanisms in Vanadium Microalloyed Steels Intended for Long Products, *ISIJ Int.*, 1998, **38**(10), p 1130–1139.
11. H. Liu, B. Yang, Y. Chen, C. Li, and C. Liu, Precipitation Law of Vanadium in Microalloyed Steel and its Performance Influencing Factors, *Materials*, 2022, **15**(22), p 8146.
12. C.A. Felker, J.G. Speer, E.D. Moor, and K.O. Findley, Hot Strip Mill Processing Simulation on a Ti-Mo Microalloyed Steel Using Hot Torsion Testing, *Metals*, 2020, **10**, p 1–19.
13. V.V. Natarajan, V.S.A. Challa, R.D.K. Misra, D.M. Sidorenko, M.D. Mulholland, M. Manohar, and J.E. Hartmann, The Determining Impact of Coiling Temperature on the Microstructure and Mechanical Properties of a Titanium-Niobium Ultrahigh Strength Microalloyed Steel: Competing Effects of Precipitation and Bainite, *Mater. Sci. Eng., A*, 2016, **665**, p 1–9.
14. R.D.K. Misra, Z. Jia, R.O. Malley, and S.J. Jansto, Precipitation Behavior During thin Slab Thermomechanical Processing and Isothermal Aging of Copper-Bearing Niobium-Microalloyed High Strength Structural Steels: The Effect on Mechanical Properties, *Mater. Sci. Eng., A*, 2011, **528**, p 8772–8780.
15. Z. Li, Z. Lv, C. Wang, L. Liu, K. Cui, and Z. Zhao, Effect of Coiling Temperature on Microstructure and Properties of Titanium Strengthened Weathering Building Steel, *Metals*, 2023, **13**, p 1–12.
16. A. Olasolo, P. Uranga, J.M. Rodriguez Ibabe, and B. Lopez, Effect of Austenite Microstructure and Cooling Rate on Transformation Characteristics in a Low Carbon Nb-V Microalloyed Steel, *Mater. Sci. Eng. A*, 2011, **528**, p 2559–2569.
17. T. Dorin, K. Wood, A. Taylor, P. Hodgson, and N. Stanford, Effect of Coiling Treatment on Microstructureal Development and Precipitate Strengthening of a Strip Cast Steel, *Acta Mater.*, 2016, **115**, p 167–177.
18. M. Olasolo, P. Uranga, J.M. Rodriguez-Ibabe, and B. López, Effect of coiling temperature on microstructure and mechanical properties of a Nb-V microalloyed steel, *Mater. Sci. Forum*, 2010, **638**, p 3350–3355.
19. Y. Lei, W. Yang, C.W. Siyasiya, and Z. Tang, Effect of Coiling Temperature on Microstructures and Precipitates in High-Strength Low-Alloy Pipeline Steel After Heavy Reduction During a six-Pass Rolling Thermo-Mechanical Controlled Process, *Metals*, 2024, **14**, p 1–17.
20. J.E. Campbell, H. Zhang, M. Burley, M. Gee, A.T. Fry, J. Dean, and T.W. Clyne, A Critical Apprasial of the Instrumented Indentation Technique and Profilometry-Based Inverce Finite element Method Indentation Plastometry for Obtaining Stress-Strain Curve, *Adv. Eng. Mater.*, 2021, **23**, p 1–13.
21. J. Wang, Q. Yang, X. Wang, and L. Wang, Effect of Coiling Temperature on Microstructure and Tensile Behavior of a Hot-Rolled Ferritic Lightweight Steel, *Metall. Mater. Trans. A*, 2016, **47A**, p 5918–5931.
22. H.K.D.H. Bhadeshia and J.W. Christian, Bainitie in steels, *Metall. Trans. A*, 1990, **21A**, p 767–797.
23. J. Wang, P.D. Hodgson, I. Bikmukhametov, M.K. Miller, and I. Timokhina, Effects of Hot-Deformation on Grain Boundary Precipitation and Segregation in Ti-Mo microalloyed Steels, *Mater. Des.*, 2018, **141**, p 48–56.
24. A. Mandal, A. Ghosh, D. Chakrabarti, and C. Davis, Effect of Coiling Temperature on Impact Toughness of Hot Rolled Ultra-High-Strength Multiphase Steel Strip, *Mater. Sci. Eng. A*, 2021, **824**, p 1–18.
25. W.J. Liu, S. Yue, and J.J. Jonas, Characterization of Ti Carbosulfide Precipitation in Ti Microalloyed Steels, *Metall. Trans. A*, 1989, **20**, p 1907–1915.
26. S. Gündüz and R.C. Cochrane, Influence of Cooling Rate and Tempering on Precipitation and Hardness of Vanadium Microalloyed Steel, *Mater. Des.*, 2005, **26**(6), p 486–492.
27. Q. Yong, X. Sun, G. Yang, and Z. Zhang, *Solution and Precipitation of Secondary Phase in Steels: Phenomenon, Theory and Practice*, Metallurgical Industry Press, Berlin, 2011
28. Z. Wu, W. Yang, Z. Tang, C.W. Siyasiya, and J. Zhang, Thermomechanical Control of Microstructure and Percipitation in Vanadium Microalloyed Steel: Influence of Finish Rolling and Coiling Temperature, *Steel Res. Int.*, 2024, **95**, p 1–10.
29. M. Sun, Y. Xu, and W. Du, Influence of Coiling Temperature on Microstructure, Precipitation Behaviors and Mechanical Properties of a Low Carbon Ti Micro-Alloyed Steel, *Metals*, 2020, **10**, p 1–10.
30. A. Karmakar, P. Sahu, S. Neogy, D. Chakrabarti, R. Mitra, S. Mukherjee, and S. Kundu, Effect of Cooling Rate and Chemical Composition on Microstructure and Properties of Naturally Cooled Vanadium-Microalloyed Steels, *Metall. Mater. Trans. A*, 2017, **48A**, p 1581–1595.
31. K. Zhang, Z.D. Li, X.J. Sun, Q.L. Yong, J.W. Yang, Y.M. Li, and P.L. Zhao, Development of Ti–V–Mo Complex Microalloyed Hot-Rolled 900-MPa-Grade High-Strength Steel, *Acta Metall. Sin.*, 2015, **28**, p 641–648.
32. P.K. Patra, S. Sam, M. Singhai, S.S. Hazra, G.D. Janaki Ram, and S.R. Bakshi, Effect of Coiling Temperature on the Microstructure and Mechanical Properties of Hot-Rolled Ti-Nb microalloyed Ultra High Strength Steel, *Trans. Indian Inst. Met.*, 2017, **70**, p 1773–1781.
33. G.E. Dieter, *Mechanical Metallurgy*, McGraw-Hill Book company, London, 1988
34. R. Abbaschian, L. Abbaschian and R.E. Reed Hill, *Physical Metallurgy Principles*, Cengage Learning, Stamford, 2009
35. H. Huang, G. Yang, G. Zhao, X. Mao, X. Gan, Q. Yin, and H. Yi, Effect of Nb on the Microstructure and Properties of Ti-Mo Microalloyed High-Strength Ferritic Steel, *Mater. Sci. Eng., A*, 2018, **736**, p 148–155.
36. Z.X. Fu, G.W. Yang, R.Y. Han, Y.W. Xu, X.P. Mao, and S.Q. Bao, Influence of Coiling Temperature on Microstructure and Mechanical Properties of Hot-Rolled High-Strength Steel Microalloyed with Ti, Mo and V, *Iron Steel Res.*, 2022, **29**, p 484–493.
37. C. Gu, C. Scott, M.J. Gaudet, F. Fazeli, J. Su, X. Wang, N. Bassim, and H. Zurob, Evolution of the Microstructure and Mechanical Properties of a V-Containing Microalloyed Steel During Coiling, *Mater. Sci. Eng., A*, 2023, **880**, p 1–11.
38. X. Gan, Q. Yuan, G. Zhao, H. Ma, W. Liang, Z. Xue, W. Qiao, and G. Xu, Quantitive Analysis of Microstructures and Strength of Nb-Ti Microalloyed Steel with Diffrent Ti Additions, *Metall. Mater. Trans. A*, 2020, **15A**, p 2084–2096.
39. S.J. Sun, Y.Z. Tian, H.R. Lin, Z.J. Wang, and Z.F. Zhang, Revisiting the Role of Prestrain History in the Mechanical Properties of Ultrafine-Grained CoCrFeMnNi High-Entropy Alloy, *Mater. Sci. Eng., A*, 2021, **801**, p 1–10.
40. K. Chen, H. Li, Z. Jiang, F. Liu, C. Kang, X. Ma, and B. Zhao, Multiphase Microstructure Formation And its Effect on Fracture Behavior of Medium Carbon High Silicon High Strength Steel, *J. Mater. Sci. Technol.*, 2021, **72**, p 81–92.
41. P.O. Guglielmi, M. Ziehmer, and E.T. Lilleodden, On a Novel Strain Indicator Based on Uncorrelated Misorientation Angles for Correlating Dislocation Density to Local Strength, *Acta Mater.*, 2018, **150**, p 195–205.